Article

Seismic evidence for partial melt below tectonic plates

Eric Debayle[1✉], Thomas Bodin[1], Stéphanie Durand[1] & Yanick Ricard[2]

The seismic low-velocity zone (LVZ) of the upper mantle is generally associated with a low-viscosity asthenosphere that has a key role in decoupling tectonic plates from the mantle[1]. However, the origin of the LVZ remains unclear. Some studies attribute its low seismic velocities to a small amount of partial melt of minerals in the mantle[2,3], whereas others attribute them to solid-state mechanisms near the solidus[4–6] or the effect of its volatile contents[6]. Observations of shear attenuation provide additional constraints on the origin of the LVZ[7]. On the basis of the interpretation of global three-dimensional shear attenuation and velocity models, here we report partial melt occurring within the LVZ. We observe that partial melting down to 150–200 kilometres beneath mid-ocean ridges, major hotspots and back-arc regions feeds the asthenosphere. A small part of this melt (less than 0.30 per cent) remains trapped within the oceanic LVZ. Melt is mostly absent under continental regions. The amount of melt increases with plate velocity, increasing substantially for plate velocities of between 3 centimetres per year and 5 centimetres per year. This finding is consistent with previous observations of mantle crystal alignment underneath tectonic plates[8]. Our observations suggest that by reducing viscosity[9] melt facilitates plate motion and large-scale crystal alignment in the asthenosphere.

Our finding results from the simultaneous analysis of two upper-mantle tomographic models of shear-wave velocity (V_s) and attenuation (parameterized by the quality factor Q_s, a measure of energy dissipation). Most global tomographic studies of the upper mantle and its thermochemical interpretation have focused on shear velocity[4,7]. Recent experiments on olivine suggest that wave speed and attenuation are insensitive to water, which implies that elevated water content is not responsible for the low-velocity zone (LVZ)[10]. However, V_s is sensitive to temperature, composition and melt content, and determining the causes of variations in V_s represents a strongly non-unique inverse problem, severely limiting our understanding of Earth's interior. Shear attenuation has a different sensitivity to these quantities and therefore provides complementary constraints on the origin of seismic heterogeneities[11]. Shear attenuation is negligibly dependent on major element chemistry[12] and exponentially dependent on temperature[13]. The relation between attenuation and melt is debated, with some experiments, models and seismological observations suggesting a weak dependence[12], while others suggest a larger effect[3]. Because measuring shear attenuation is difficult, only a few global Q_s models have been published in the past 20 years[14]. The only recent joint interpretation of three-dimensional Q_s and V_s tomographic models at a global scale is based on models built from different datasets and modelling approaches[15].

The novelty of our approach is that we simultaneously interpret two recent global V_s and Q_s models, which are obtained from the same Rayleigh-wave dataset, at the same resolution and using the same modelling approach, and are therefore consistent. These V_s (DR2020s) and Q_s (QsASR17) models are displayed in Fig. 1. Details of our tomographic procedure are provided in Methods. Before interpreting these two models in light of laboratory experiments, we consider the temperature and pressure ranges for which our interpretation applies. The attenuation models derived from mineral physics[4,13] are valid for temperatures T larger than 900 °C, which corresponds to the base of the lithosphere and to the asthenosphere. These models consider thermally activated processes that vary exponentially as $1/T$, implying quality factors in excess of 2,000 in the upper 100 km of the lithosphere and reaching several million near the surface (Methods). However, finite Q_s is observed in the crust and in the cold mantle lithosphere, where attenuation is most probably related to non-thermal processes such as scattering or fluid–fracture interactions[14]. Furthermore, the attenuation observed in seismology accumulates along the seismic ray and the observation of Q_s is possible only when the amplitude of a wave is measurably smaller than in a pure elastic model. Given the uncertainties on amplitude data, it seems impossible to resolve quality factors larger than around 2,000 with long-period Rayleigh waves (at periods of 100 s, assuming velocities of 4.5 km s^{-1} and ray lengths of 10,000 km, the amplitude reduction with respect to a pure elastic model, would be less than 3.5%). Our inversion leads to a Q_s model with strong lateral variations (two orders of magnitude), but with a maximum Q_s of about 1,750. Our attenuation model is therefore mostly adapted to depths of at least about 100 km, where Q_s values between 50 and a few hundred are expected[15]. Our interpretation therefore applies to the oceanic asthenosphere and the mantle structure at depths of at least about 100 km, where our tomographic models are accurate and where conditions similar to those used in laboratory experiments exist.

Figure 2 displays Q_s as a function of V_s for each pixel of the maps, at different depths in the upper mantle. The curves in dark and light blue represent the theoretical relations due to temperature variations for a

[1]Univ Lyon, Univ Lyon 1, ENSL, CNRS, LGL-TPE, Villeurbanne, France. [2]Univ Lyon, ENSL, Univ Lyon 1, CNRS, LGL-TPE, Lyon, France. ✉e-mail: Eric.Debayle@ens-lyon.fr
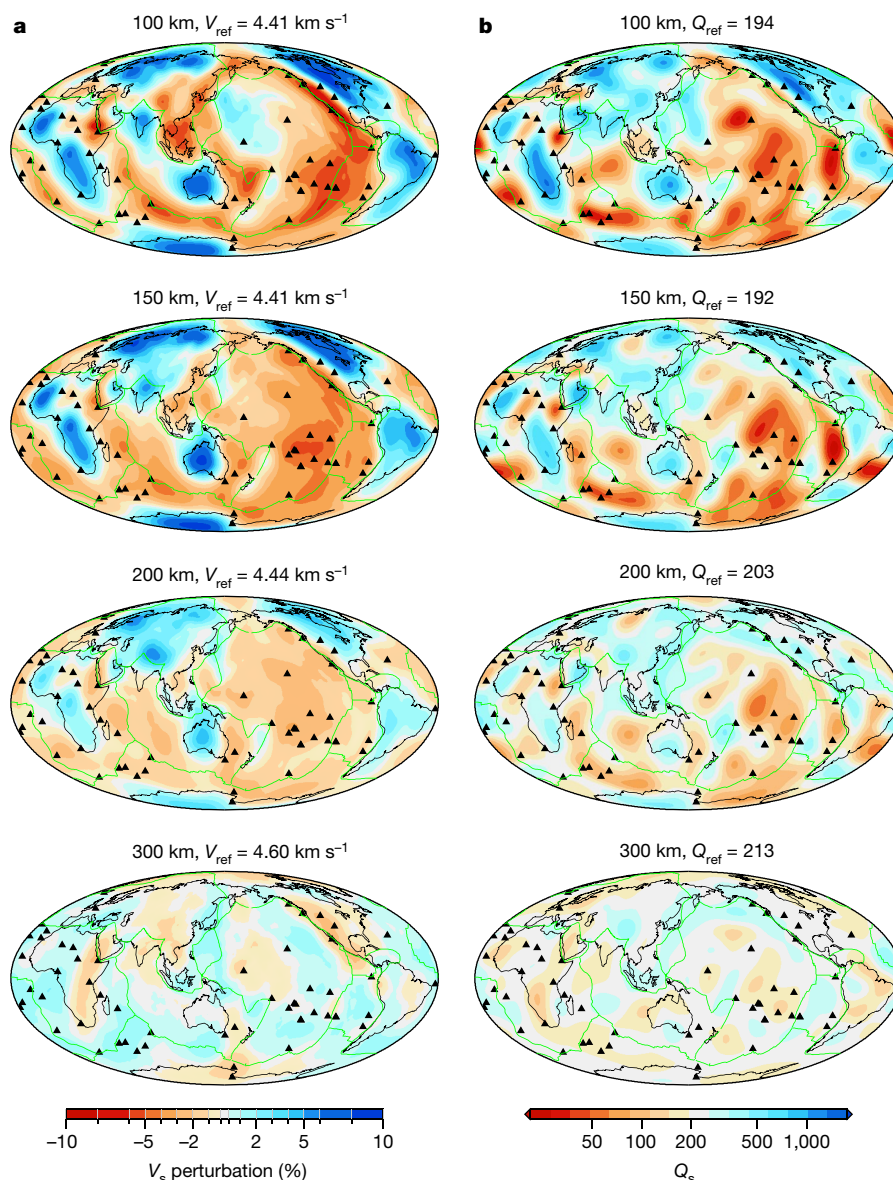
Fig. 1 | Shear velocity and attenuation in the upper mantle. a, Perturbations (%) in V_s from DR2020s with respect to a mean value V_{ref}. **b**, Maps of our Q_s tomographic model QsADR17 at different depths in the upper mantle. Q_s is plotted using a logarithmic scale. Its geometric average is given above the colour scale. Hotspot locations are shown with black triangles.

meltless pyrolytic mantle[16], given by two anelasticity models[4,13] based on laboratory experiments, appropriate for asthenospheric conditions (Methods). These models explain only a limited part of the velocities and attenuations of our dataset. We consider the first theoretical curve[4] to be compatible with a given V_s–Q_s observation if it falls within the typical uncertainties of the V_s and $\ln Q_s$ observations, of 1% and 10%, respectively (ivory colour). We show in Methods and Supplementary Figs. 1–10 that the low values of V_s cannot be reconciled with Q_s by adding radial anisotropy, elastically accommodated grain-boundary sliding, or the effect of composition or water. However, they can be reconciled by adding partial melt, which reduces V_s and shifts the theoretical curves to the left in Fig. 2, but has little effect on Q_s, as discussed below. Warm colours in Fig. 2 indicate the amount of melt (less than 0.7%) needed to reconcile observations with the first theoretical model[4] (dark blue curve), which requires the smallest amount of melt. On the right side of the ivory region, points in grey are those for which V_s is too high compared to the theoretical value. These points are associated with the lithospheric depletion of cratonic roots. In this case, the

grey intensity quantifies the departure (in per cent) from the theoretical curve, assuming a meltless pyrolytic mantle. Results using the second theoretical model[13] are shown in Supplementary Figs. 11 and 12. These results lead essentially to the same conclusions, but require larger melt fractions (up to 1%), which are more difficult to reconcile with the very small melt fraction (roughly 0.1%) suggested by geochemical studies[4].

On the basis of model calculations[17], V_s has been estimated to reduce by 7.9% for each 1% of melt. Recent experiments[3] are in qualitative agreement with this model prediction, but require a slightly larger reduction in V_s (Supplementary Fig. 13). The effect of melt on attenuation is not well constrained and depends on the mechanisms of attenuation. We show in Methods that melt may have a large effect on Q_s at short periods (1 s), but not in the period range of surface waves (50–250 s). We therefore neglect the effect of melt on Q_s and model its effect on V_s on the basis of recent experiments[3]. Figure 2 shows that the slowest shear velocities require less than 0.7% of melt.

Figure 3 displays global maps of melt content at different depths, using the same colour-coding as in Fig. 2. The associated mantle
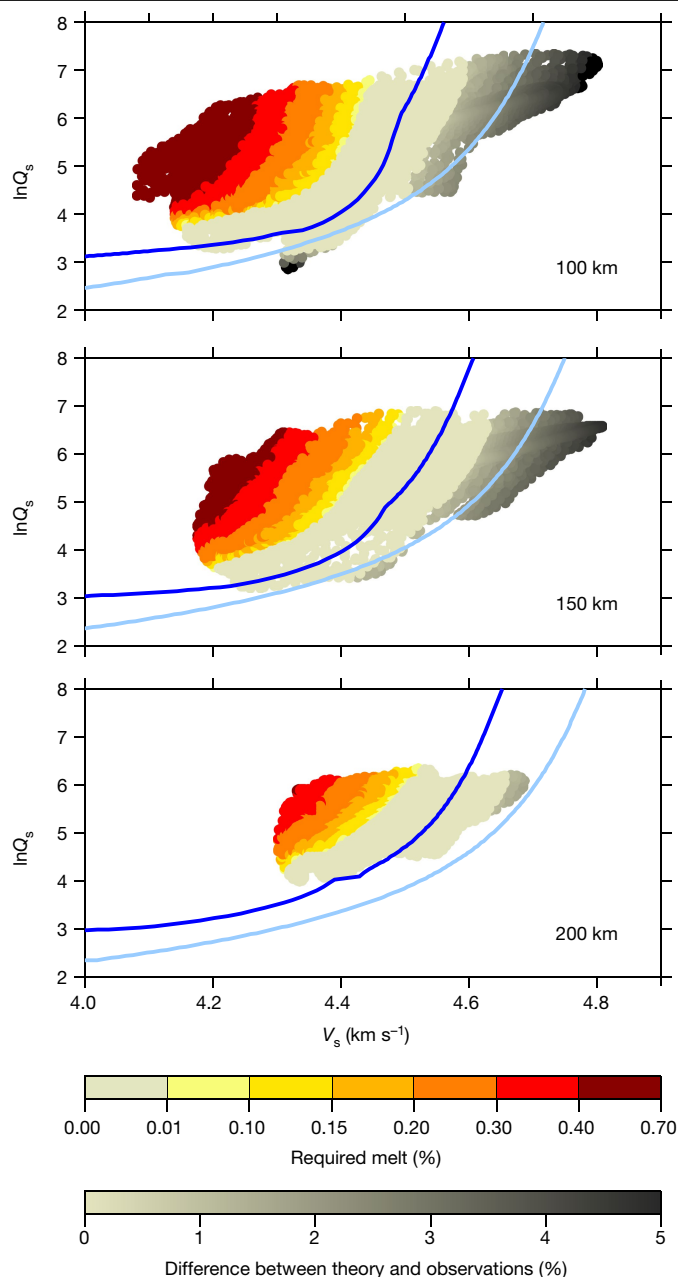
Fig. 2 | Observed shear attenuation as a function of shear velocity, compared with theoretical predictions. The velocities (V_s; from DR2020s) and attenuation values ($\ln Q_s$; from QsADR17) are plotted at 100-km, 150-km and 200-km depth. Each point corresponds to a geographical location. The dark and light blue curves are the theoretical predictions assuming a pyrolitic composition[16] in the absence of melt, using the anelasticity models from ref. [4] and ref. [13], respectively. The upper colour scale indicates the amount of melt (%) required to explain our observations using the model from ref. [4]. Adding melt lowers the predicted V_s without changing Q_s. The lower colour scale indicates the difference (%) between theory and observations, in regions where V_s is too high and cannot be reconciled with model predictions assuming a pyrolitic mantle.

temperatures, derived using our approach, are on average slightly above the solidus in oceanic regions, between depths of 100 km and 200 km (Supplementary Fig. 14g). The differences between the maps of temperature (Supplementary Fig. 14a–f) and those of melt content are attributed to a variable amount of volatiles[9]. More volatiles above subduction zones may lower the solidus and favour melting, whereas a dryer mantle in other regions may impede melting. The heterogeneities

in Fig. 3 display a strong correlation with surface tectonics. Regions where V_s is too high (grey) are located beneath continents down to depths of 150 km. The discrepancy is probably due to our assumption of a homogeneous and pyrolitic mantle. This assumption is reasonable in the well-mixed convective mantle. However, beneath cratons, compositional heterogeneities and depletion of incompatible elements contribute to the high seismic velocities. Our observations under cratons, at a depth of 150 km, correspond to velocities on average 2.4% faster than those for a pyrolitic mantle, which is consistent with compositional effects[18].

At a depth of 100 km, melt is required below mid-ocean ridges, some hotspots near the Atlantic ridge and in the south Pacific Ocean, back-arc basins around the Pacific Ocean, including the eastern margin of Asia, and some other active tectonic regions (Afar, Tibet, west of North America and the southwest Pacific, including the north Fidji basin and the Northfolk ridge south of the Vanuatu arc). In these regions, the amount of melt exceeds 0.3% and can reach 0.7%. Melt is not required beneath most of the remaining oceanic and continental Phanerozoic lithosphere, where temperature variations alone explain our observations.

The depth range 150–200 km corresponds to the oceanic LVZ, where a small amount of melt (less than 0.3%) is required over broad regions. The largest amount is beneath hotspots, ridges and volatile-rich back-arc regions, and can extend deeper than the LVZ, suggesting that these deep regions feed the asthenosphere with partial melt. For example, partial melt is observed down to 250 km beneath Hawaii and 300 km beneath the Afar and east African rifts, the hotspots located on the western part of North America, the region of the Balleny Islands in Antarctica, the western Pacific and the Indian ocean near the Ninety East ridge. A melting anomaly near 300 km on the eastern part of the Tibetan plateau is also observed.

The depth extent and amount of melt beneath oceanic regions are consistent with local studies. The NoMELT experiment[19] was performed beneath a location relatively far away from Pacific hotspots (blue stars in Fig. 3), where we too confirm the absence of melt in what could be a volatile-poor mantle. We observe melting beneath the East Pacific Rise (green stars in Fig. 3) down to 250-km depth, in agreement with the MELT experiment[20]. The depth extent of melting beneath Hawaii, down to 250 km, is supported by measurements of water abundance in the deep region that feeds the plume[21]. Our results agree with observations of substantial melting beneath the Philippine Sea plate and the western Pacific[2]. Finally, melting down to at least 300 km beneath the Balleny Islands hotspot is also consistent with previous observations[22].

The origin of partial melt within most of the oceanic LVZ is uncertain. Melting at mid ocean-ridges can exceed 1% in the depth range 40–80 km (refs. [20,23]), but smaller volume melting may occur down to depths of 150–250 km (ref. [23]). After melting at mid-ocean ridges, a small amount of melt may remain unextractable from the mantle peridotite[9,24,25]. Our observations suggest that decompression melting with at least 0.3%–0.7% of melt also occurs beneath some hotspots and back-arc basins down to about 200 km. Most of the melt produced in these regions is extracted and incorporated into the oceanic crust, but a small amount remains in the oceanic LVZ as it ages. The quantity of melt, if any, decreases close to continents, to below 0.1%, where a simple model without melt explains most of our observations. This may be due to the difficulty of melting the depleted continental lithosphere. However, under tectonically active regions, beneath the Afar and east African rifts, Tibet, western North America and the Transantarctic mountains, the asthenosphere contains a small amount of melt (Fig. 3).

The quantity of melt needed to reconcile V_s and Q_s under large swaths of the oceanic LVZ is larger than usual estimates of unextractable melt, which range from very small values[9] to a maximum of 0.1%[24]. Although melt is probably connected and able to percolate even at very small porosity[9], surface tension resists the phase separation[9,26]. The ability
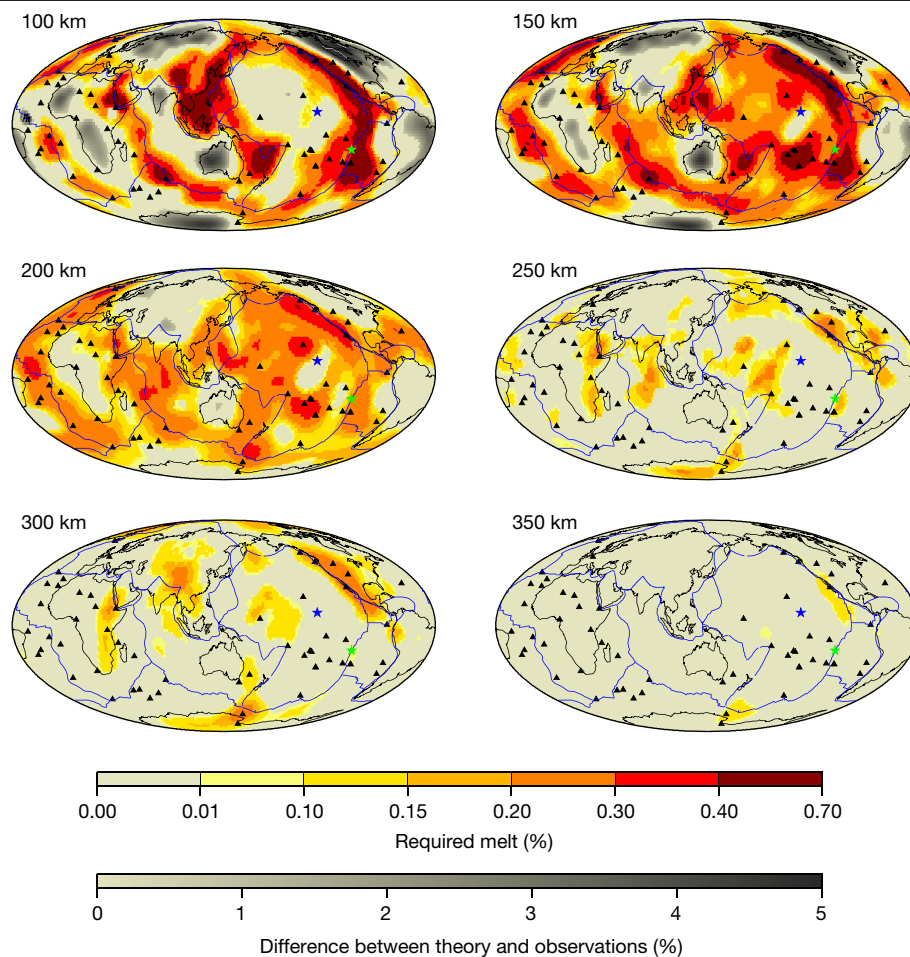
Fig. 3 | Melt content at different depths in the upper mantle. This melt content is derived from the joint interpretation of QsADR17 and DR2020s. The colour scales are the same as in Fig. 2. Hotspot locations are indicated with black triangles. The blue and green stars indicate the locations of the NoMELT and MELT experiments, respectively.

of the melt to rise depends on various parameters—surface tension, buoyancy, permeability, melt and matrix viscosities—which all have large uncertainties[25]. The melt fractions greater than 0.1% that we obtain are therefore plausible. This melt concentration is in overall agreement with the range of estimates derived from electromagnetic studies[27] of the LVZ, which often propose even larger values (Methods). A structure made of magma-rich sills embedded in a meltless mantle might also be mapped by tomography as an average medium with moderate melt content. This partially molten layered model has been proposed for the northwest Pacific and Philippine plates[2], but it could extend more generally to the entire oceanic LVZ. This layering would explain both the radial anisotropy observed within the oceanic LVZ[28] and the sharp velocity and viscosity contrasts at the lithosphere–asthenosphere boundary[2].

Finally, the amount of melt exhibits an unexpected relation with the plate velocity[29] expressed in a no-net-rotation reference frame (Fig. 4). The melt fraction in the asthenosphere increases abruptly, by a factor close to 2, when the velocity is larger than 4 cm yr^{-1}. This variation is very similar to the observed variation of azimuthal anisotropy with present-day plate motion[8]. Our results suggest that plate-scale crystal alignment beneath fast-moving plates is associated with a greater amount of melt. This requires that melt facilitates deformation[9] and/or that deformation favours melt retention in the LVZ[2]. In any case, the small amount of melt observed beneath large swaths of the oceanic LVZ is likely to decrease viscosity substantially (by one to two orders of magnitude[9]; Methods) and to have an important role in the decoupling of tectonic plates from the mantle.
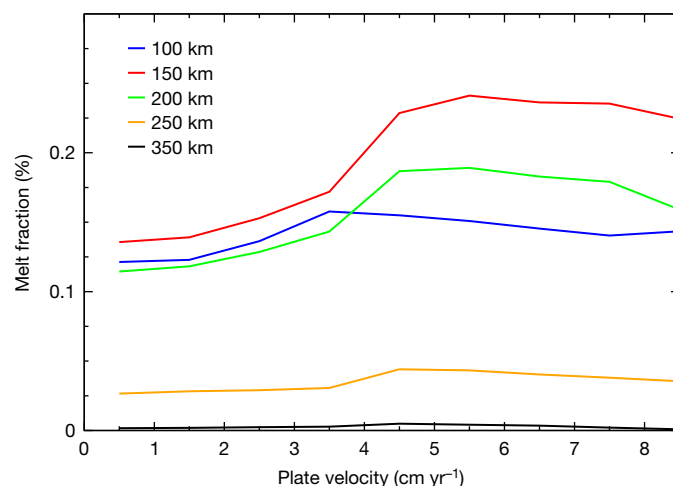

Fig. 4 | Melt fraction at different depths as a function of absolute plate velocity. The velocities[29] are expressed in a no-net-rotation reference frame. The melt fraction (%) is averaged for all geographical points with similar plate velocities, using a sliding window of ±2 cm yr^{-1}. The amount of melt increases substantially in the asthenosphere (100–200 km) for plate velocities between 3 cm yr^{-1} and 5 cm yr^{-1}. This result links with previous observations that only plates moving faster than 4 cm yr^{-1} can organize the flow at a large scale in the underlying asthenosphere[8], suggesting that melt reduces viscosity[9] and facilitates large-scale crystal alignment.

Online content

Any methods, additional references, Nature Research reporting summaries, source data, extended data, supplementary information, acknowledgements, peer review information; details of author contributions and competing interests; and statements of data and code availability are available at https://doi.org/10.1038/s41586-020-2809-4.

1. Ricard, Y., Doglioni, C. & Sabadini, R. Differential rotation between lithosphere and mantle: a consequence of lateral mantle viscosity variations. *J. Geophys. Res*. **96**, 8407–8415 (1991).
2. Kawakatsu, H. et al. Seismic evidence for sharp lithosphere-asthenosphere boundaries of oceanic plates. *Science* **324**, 499–502 (2009).
3. Chantel, J. et al. Experimental evidence supports mantle partial melting in the asthenosphere. *Sci. Adv.* **2**, e1600246 (2016).
4. Takei, Y. Effects of partial melting on seismic velocity and attenuation: a new insight from experiments. *Annu. Rev. Earth Planet. Sci.* **45**, 447–470 (2017).
5. Faul, U. H. & Jackson, I. The seismological signature of temperature and grain size variations in the upper mantle. *Earth Planet. Sci. Lett.* **234**, 119–134 (2005).
6. Karato, S.-i. On the origin of the asthenosphere. *Earth Planet. Sci. Lett.* **321–322**, 95–103 (2012).
7. Cobden, L., Trampert, J. & Fichtner, A. Insights on upper mantle melting, rheology, and anelastic behavior from seismic shear wave tomography. *Geochem. Geophys. Geosyst.* **19**, 3892–3916 (2018).
8. Debayle, E. & Ricard, Y. Seismic observations of large-scale deformation at the bottom of fast-moving plates. *Earth Planet. Sci. Lett.* **376**, 165–177 (2013).
9. Holtzman, B. K. Questions on the existence, persistence, and mechanical effects of a very small melt fraction in the asthenosphere. *Geochem. Geophys. Geosyst.* **17**, 470–484 (2016).
10. Cline, C. J., Faul, U. H., David, E. C., Berry, A. J. & Jackson, I. Redox-influenced seismic properties of upper-mantle olivine. *Nature* **555**, 355–358 (2018).
11. Deschamps, F., Konishi, K., Fuji, N. & Cobden, L. Radial thermo-chemical structure beneath western and northern Pacific from seismic waveform inversion. *Earth Planet. Sci. Lett.* **520**, 153–163 (2019).
12. Shito, A., Karato, S.-i., Matsukage, K. N. & Nishihara, Y. in *Earth's Deep Water Cycle* (eds Jacobsen, S. D. & Van Der Lee, S.) 255–236 (AGU, 2006).
13. Jackson, I., Fitz Gerald, J. D., Faul, U. H. & Tan, B. H. Grain-size-sensitive seismic wave attenuation in polycrystalline olivine. *J. Geophys. Res. Solid Earth* **107**, 2360 (2002).
14. Romanowicz, B. A. & Mitchell, B. J. in *Treatise on Geophysics* 2nd edn (ed. Schubert, G.) 789–827 (Elsevier, 2015).
15. Dalton, C. A., Ekström, G. & Dziewonski, A. M. Global seismological shear velocity and attenuation: a comparison with experimental observations. *Earth Planet. Sci. Lett.* **284**, 65–75 (2009).
16. Xu, W., Lithgow-Bertelloni, C., Stixrude, L. & Ritsema, J. The effect of bulk composition and temperature on mantle seismic structure. *Earth Planet. Sci. Lett.* **275**, 70–79 (2008).
17. Hammond, W. C. & Humphreys, E. D. Upper mantle seismic wave velocity: effects of realistic partial melt geometries. *J. Geophys. Res. Solid Earth* **105**, 10975–10986 (2000).
18. Bruneton, M. et al. Layered lithospheric mantle in the central Baltic Shield from surface waves and xenolith analysis. *Earth Planet. Sci. Lett.* **226**, 41–52 (2004).
19. Lin, P. Y. P. et al. High-resolution seismic constraints on flow dynamics in the oceanic asthenosphere. *Nature* **535**, 538–541 (2016).
20. Yang, Y., Forsyth, D. W. & Weeraratne, D. S. Seismic attenuation near the East Pacific Rise and the origin of the low-velocity zone. *Earth Planet. Sci. Lett.* **258**, 260–268 (2007).
21. Wallace, P. J. Water and partial melting in mantle plumes: Inferences from the dissolved H_2O concentrations of Hawaiian basaltic magmas. *Geophys. Res. Lett.* **25**, 3639–3642 (1998).
22. Sieminski, A., Debayle, E. & Lévêque, J.-J. Seismic evidence for deep low-velocity anomalies in the transition zone beneath West Antarctica. *Earth Planet. Sci. Lett.* **216**, 645–661 (2003).
23. Key, K., Constable, S., Liu, L. & Pommier, A. Electrical image of passive mantle upwelling beneath the northern East Pacific Rise. *Nature* **495**, 499–502 (2013).
24. Faul, U. H. Melt retention and segregation beneath mid-ocean ridges. *Nature* **410**, 920–923 (2001).
25. Selway, K. & O'Donnell, J. P. A small, unextractable melt fraction as the cause for the low velocity zone. *Earth Planet. Sci. Lett.* **517**, 117–124 (2019).
26. Hier-Majumder, S., Ricard, Y. & Bercovici, D. Role of grain boundaries in magma migration and storage. *Earth Planet. Sci. Lett.* **248**, 735–749 (2006).
27. Ni, H., Keppler, H. & Behrens, H. Electrical conductivity of hydrous basaltic melts: implications for partial melting in the upper mantle. *Contrib. Mineral. Petrol.* **162**, 637–650 (2011).
28. Chang, S.-J. J., Ferreira, A. M. G. G., Ritsema, J., van Heijst, H. J. & Woodhouse, J. H. Joint inversion for global isotropic and radially anisotropic mantle structure including crustal thickness perturbations. *J. Geophys. Res. Solid Earth* **120**, 4278–4300 (2015).
29. DeMets, C., Gordon, R. G., Argus, D. F. & Stein, S. Effect of recent revisions to the geomagnetic reversal time-scale on estimates of current plate motions. *Geophys. Res. Lett.* **21**, 2191–2194 (1994).

Article

Methods

Q_s and V_s tomographic models

Figure 1 presents maps of DR2020s, our global V_s model, and QsADR17, a recent global Q_s model[30]. Both models are built from the same massive Rayleigh-wave measurements[31] and obtained using a similar tomographic procedure. The first step is an automated waveform inversion approach, which was applied to approximately 375,000 Rayleigh seismograms[31]. From a single surface-wave seismogram, the waveform inversion extracts simultaneously a path-average depth-dependent shear-velocity profile, V_s, and quality factor, Q_s. By jointly interpreting the amplitude and phase of each waveform, we ensure that the interplay between V_s and Q_s is accounted for, and that the shear quality factor and velocity profiles are constrained within the same period range. The waveform analysis is performed in the period range 50–250 s and accounts for the fundamental and up to the fifth higher mode of Rayleigh waves, thus ensuring a good depth resolution for V_s and Q_s from 50-km depth down to the transition zone. It is a nonlinear iterative process, which also produces frequency-dependent phase velocity and attenuation curves compatible with the recorded waveform. The effect of physical dispersion due to attenuation is accounted for in the modelling.

The second step is a regionalization of the one-dimensional path-average models. DR2020s is obtained from the regionalization at each depth of the path-average V_s models using a continuous regionalization approach[31]. This tomographic inversion yields three-dimensional absolute velocities. QADR17, a global model of Rayleigh-wave attenuation, was obtained after adapting the same regionalization approach to our dataset of Rayleigh-wave attenuation curves, parameterized as $\ln Q$ (ref. [32]). The regionalization of the path-average attenuation curves accounts for frequency-dependent effects such as focusing–defocusing, which can have important effects on the amplitude of Rayleigh waves. The logarithmic parameterization brings the distribution of the quality-factor dataset close to a Gaussian, allows the large variations in Q documented by local seismic studies and avoids negative attenuation values in the inverted model. The horizontal smoothing in DR2020s and QADR17 is determined by a Gaussian a priori covariance function controlled by an angular correlation length. In ref. [32], a conservative value of 10° was chosen (meaning that the Q model is resolved accurately up to spherical harmonic 12). In ref. [31], a shorter correlation length of 3.6° was used for the V_s model DR2012. We re-inverted the dataset from ref. [31] using a correlation length of 10° to obtain an SV-wave tomographic model at the same horizontal resolution and vertical smoothing as QsADR17. To minimize biases due to un-modelled radial anisotropy, we computed the isotropic Voigt average of our SV model and the SH model obtained by adding the radial anisotropy of PREM to our SV model. The resulting isotropic model (DR2020s) is plotted in Fig. 1. Using other one- or three-dimensional models of radial anisotropy does not affect our conclusions, as discussed below. QsADR17 was obtained from the inversion at depth of QADR17[30], using the same vertical smoothing as for DR2020s. DR2020s and QsADR17 are therefore consistent because they are derived from the simultaneous inversion of the same waveforms and inverted using the same regionalization approach with the same Gaussian filtering.

Prediction of Q_s and V_s using a temperature-dependent model[4]

The dark blue curve in Fig. 2 is obtained by predicting V_s and Q_s at each depth for a range of temperatures, using a temperature-dependent anelasticity model[4] and assuming a pyrolytic composition[16]. This model parameterizes the relaxation spectrum with a small number of variables determined from experimental data. It accounts for a monotonic background spectrum plus a broad temperature-dependent absorption peak in the seismic frequency band, the amplitude and width of which increase below the solidus. This produces a substantial enhancement of polycrystal anelasticity before melting. This pre-melting effect greatly reduces V_s under the solidus. We choose the solidus according to ref. [33]. We use the model parameters given in tables 1 and 2 of ref. [4], except for the unrelaxed shear modulus μ_u. We estimate μ_u for a pyrolytic mantle using the mineralogic phase diagram computed by the Perple X software[34]. In Supplementary Figs. 15 and 16, we show the results obtained with the shear modulus of ref. [4], which reduces the amount of melt in oceanic regions but does not explain our $\ln Q_s$–V_s observations beneath old oceanic basins at 100-km depth. It also substantially increases the misfit beneath continents.

Prediction of Q_s and V_s from experimental results[13]

The light blue curve in Fig. 2 is obtained using a two-step process. First, we use experimental results on melt-free polycrystalline olivine to predict a theoretical quality factor Q_t. Computations are performed in the temperature range 800–1,800 K and pressure range 1.49–12.99 GPa, corresponding to the depth range 50–390 km. We use the following relation[13]:

$$Q_t^{-1}(T_0, T, P, d) = A\left[\frac{T_0}{d}\exp\left(-\frac{E+PV}{RT}\right)\right]^\alpha. \qquad (1)$$

In this formulation, Q_t^{-1} at period T_0 depends on the temperature T, the pressure P and to a lesser extent the grain size d; R is the gas constant, E is the activation energy and V is the activation volume. Supplementary Table 1 summarizes the values of the different parameters in equation (1). In the range of values compatible with experiments[13], we choose $T_0 = 100$ s, the average period of our long-period Rayleigh waves and $d = 0.01$ m. The theoretical curves corresponding to equation (1) are shown in Supplementary Fig. 9, with the effect of changing grain size.

Second, we use Perple X (ref. [34]) to estimate an isotropic V_s for a pyrolytic model[16]. We compute V_s for the same temperatures and pressures as Q_t. Perple X produces unrelaxed S-wave velocities at infinite frequency, above the absorption band of seismic attenuation, whereas our long-period (>50 s) seismic surface waves are likely to have relaxed velocities. We therefore correct for the effect of anelasticity on V_s (ref. [35]):

$$V_{s,t} = V_{s\infty}\left[1 - \frac{Q_t^{-1}(T_0, T, P, d)}{2\tan(\pi\alpha/2)}\right], \qquad (2)$$

where $V_{s\infty}$ is the unrelaxed velocity and $V_{s,t}$ is the velocity corrected for the effect of attenuation. According to equation (2), the stronger the attenuation, the stronger the velocity reduction. The light blue curve in Fig. 2 is then obtained by plotting, at a given depth, the obtained $\ln Q_t$ as a function of $V_{s,t}$ for each temperature.

Comparison between observations and theoretical relations

At each geographical location and depth, we extract the observed values of Q_s in QsADR17 and V_s in DR2020s and compare these with the chosen theoretical relation. We consider a theoretical curve to be compatible with a given V_s–Q_s observation if it falls within ±1% and ±10% of the V_s and $\ln Q_s$ observations, respectively (Fig. 2). These errors are on the conservative side of recent estimates[36,37]. If the theoretical relation cannot explain our observations, two situations can arise. First, the observed V_s is lower than the theoretical $V_{s,t}$, in which case melt can be added to reduce $V_{s,t}$. This is done assuming melt has no effect on Q_s. Second, the observed V_s is higher than $V_{s,t}$. This is mostly the case under continents and can be explained by the depletion of the pyrolytic mantle increasing the theoretical $V_{s,t}$ (ref. [18]).

Effect of grain size

Grain sizes in the shallow upper mantle are probably 1–20 mm, as observed in upper-mantle xenoliths, harzburgite and dunite bodies[13]. The effect of grain size on equation (1) is shown in Supplementary Fig. 9. The blue areas around the theoretical curves cover the

influence of grain size from 1 mm (bottom dotted curve) to an upper bound of 100 mm (upper dashed curve). For a given Q_s, increasing the grain size increases the temperature and therefore decreases the velocity. As melt is required to explain slow velocities, increasing the grain size decreases the amount of melt required to explain our observations. Using equation (1), we show melt distributions obtained for $d = 0.01$ m (Supplementary Fig. 12) and for the extreme value $d = 0.1$ m (Supplementary Fig. 17), which minimizes the amount of melt required in the LVZ. The maps in Supplementary Fig. 17 are similar to those in Supplementary Fig. 12 with a smaller amount of melt. However, in both cases, amounts of melt are larger than for our preferred model using the equations from ref. [4] (Fig. 3).

Amounts of melt
Although the amount of melt in the LVZ depends on the choice of the anelasticity model and on the effect of melt on V_s, we show (Supplementary Figs. 12, 16–18) that different choices of parameters yield similar maps and that melt fractions away from source regions always stay below 1%, in agreement with the partially molten asthenosphere model[2]. However, our preferred anelasticity model[4] generally explains our V_s and $\ln Q_s$ observations without the need for partial melt above and below the asthenosphere (Fig. 3). This is therefore a conservative choice, able to reconcile our V_s and $\ln Q_s$ observations in most of the upper mantle, while minimizing the amount of melt required in the LVZ.

Effect of radial anisotropy
We used the anisotropic parameter $\xi = (V_{SH}/V_{SV})^2$ of PREM to convert our SV observations into an isotropic model (DR2020s). We checked that three-dimensional models of ξ obtained from anisotropic models such as SEMUM2[38] or S362ANI[39] would not affect our main conclusions. As an example, Supplementary Fig. 1 is similar to Fig. 3, but based on our SV observations corrected with the anisotropic ξ parameters of SEMUM2 (Supplementary Fig. 2). Only minor changes are observed (for example, in the Pacific or Indian oceans at 150 km and 200 km), but none that would change our interpretations. The lateral variations in ξ in SEMUM2 (Supplementary Fig. 2) are too small to affect our results. To confirm this, we computed the anisotropy ξ that would be needed to account for the discrepancy between observed Q_s and V_s, without including mantle depletion or partial melt (Supplementary Fig. 3). Comparison of this figure with Supplementary Fig. 2 shows that neither the patterns nor the amplitude would fit (an anisotropy 3–4 times larger than in SEMUM2 would be needed to explain our observations). Therefore, the anisotropy does not affect our conclusions.

Elastically accommodated grain boundary sliding (EAGBS) hypothesis
Anelastic relaxation caused by EAGBS can produce a sharp velocity reduction and may explain the lithosphere–asthenosphere boundary and the mid-lithosphere discontinuity observed beneath continents[40]. We tested the EAGBS hypothesis as an alternative explanation to partial melting for reconciling V_s and Q_s in the LVZ. EAGBS is characterized by a sharp attenuation peak at a characteristic frequency ω_{EAGBS}, followed by a diffuse absorption band at lower frequencies. We first compute the characteristic frequency for the transition between unrelaxed and relaxed shear moduli[40]:

$$\omega_{EAGBS} = \frac{A}{d}\exp\left(-\frac{E^* + PV^*}{RT}\right)\left[1 + \left(\frac{C_w}{C_{w0}}\right)^r\right], \qquad (3)$$

where C_w is the water content (wt%), $A = 2.3 \times 10^{-14}$ m s^{-1}, $C_{w0} = 10^{-4}$ wt%, $r = 1$, $E^* = 350$ kJ mol^{-1}, $V^* = 10^{-6}$ m^3 and $d = 5 \times 10^{-3}$ m. Following ref. [7], we assume a dry mantle with $C_w = 10^{-6}$ wt%.

Surface waves analysed at frequencies lower than ω_{EAGBS} should have relaxed velocities within the absorption band (see figure SI-2 of ref. [40]), provided that the depth and temperature are within the activation ranges of EAGBS (60–160 km, 900–1,350 K). We consider that EAGBS may affect the interpretations of our long-period (>40 s) Q_s and V_s maps when $\omega_{EAGBS} > 0.025$ Hz and, from figure 4 of ref. [40], in the following temperature ranges for the depths of our tomographic inversion: 70 km, 930–1,140 K; 90 km, 980–1,180 K; 100 km, 1,010–1,220 K; 125 km, 1,060–1,270 K; 150 km, 1,130–1,330 K.

Regions where EAGBS can apply are displayed in green in Supplementary Fig. 4. These regions correspond mostly to continental areas. Assuming that EAGBS correction applies, ref. [40] provides three alternative formulations for the velocity reduction. The Ghahremani equation[41], which produces the smallest velocity reduction is

$$V_s^{EAGBS} = V_{s,t}\sqrt{\frac{0.86 - 0.83\nu}{1 - \nu}\frac{1 + \nu}{1.14 + 0.83\nu}}, \qquad (4)$$

where ν is Poisson's ratio (roughly 0.3 for upper-mantle minerals). Regions where this can reconcile our V_s and Q_s observations are displayed in red in Supplementary Fig. 4. The two other formulations give too large velocity reductions. Supplementary Fig. 4 shows that EAGBS does not reconcile our long-period observations, except in a few localized regions (in red). This does not preclude EAGBS from having an important role in explaining the sharp velocity reduction associated with the lithosphere–asthenosphere boundary, which cannot be resolved by long-period surface waves. However, the strong velocity reduction observed within the LVZ requires another mechanism.

Effect of composition
Compositional heterogeneities exist in the upper mantle, probably in the domain limited by pyrolite, harzburgite and pyroxenite[42]. We check the effect of changing the composition from pyrolite to these end members, using Perple X (ref. [34]) to compute the velocities. Pyroxenites have variable bulk compositions[43]; we consider both a silica-deficient composition (table 1 of ref. [44]) and a silica-excess composition similar to that of a subducted basalt (table 1 of ref. [16]). A silica-excess pyroxenite would be faster than pyrolite only after eclogitization, below 150-km depth (Supplementary Fig. 5, orange curve). At 100-km depth, a mantle made entirely of silica-excess pyroxenite would be too slow to explain the observed velocities (Supplementary Fig. 6). At larger depth, after eclogitization, it would lead to large melt fractions (Supplementary Fig. 6). The silica-deficient pyroxenite and the harzburgite are characterized at asthenospheric conditions by much faster or comparable velocities than pyrolite (Supplementary Fig. 5) and hence cannot explain the low velocities that we attribute to the presence of melt. Harzburgite would give melt fractions and distribution similar to pyrolite (Supplementary Fig. 7), whereas the silicate-deficient pyroxenite would lead to higher melt fractions (up to 1.7%) and a ubiquitous melt presence below 150-km depth (Supplementary Fig. 8). Pyroxenite, whether enriched or depleted in silica, should be present only in a small proportion (about 5%)[42] that hardly affects the seismic velocities of the peridotitic mantle. At any rate, large-scale chemical heterogeneities (>1,000 km) are not likely to exist in the LVZ, where viscosity is small (below 10^{20} Pa s) and the convective mantle should be well stirred and mixed. Therefore, our observations cannot be explained by reasonable variations in composition in the LVZ.

Possible effect of water
Although, it has recently been shown that, in olivine, wave speed and attenuation are insensitive to water[10], previous studies suggest an effect of water quantified by[45]

$$Q_t^{-1}(T_0, T, P, C_{OH}, d) = A\left[\frac{T_0}{d}\left(\frac{C_{OH}}{C_{OH(ref)}}\right)^r \exp\left(-\frac{E + PV}{RT}\right)\right]^\alpha, \qquad (5)$$

Article

where C_{OH} is the water concentration, r is a dimensionless constant and all other parameters are as in equation (1). The average H_2O content of Earth's upper mantle is estimated[46] to be 50–200 ppm. We test a value close to the upper bound ($C_{OH} = 10^3H/10^6Si$, corresponding to 125 ± 75 ppm by weight of water) with $r = 1$, a standard value for moderate water content and $C_{OH(ref)} = 50H/10^6SI$ (ref. [7]). The corresponding theoretical curves are shown in blue in Supplementary Fig. 9. At fixed temperature, water increases attenuation. However, to keep Q constant, an increase in water content must be balanced by a decrease in temperature and therefore by a higher expected velocity $V_{s,t}$. Reconciling this higher $V_{s,t}$ with our observations requires larger amounts of melt (Supplementary Fig. 10). Therefore, if there were an effect of water on V_s and Q_s, it would increase the required amount of melt.

Effect of melt on attenuation

A small amount of melt might have a large effect on attenuation[47] in the case of grain-boundary sliding, where a broad dissipation peak is observed in the seismic frequency band. Body-wave studies have reported low Q_s values at short period (1s), with $Q_s \leq 25$ beneath the Juan de Fuca and Gorda ridges[48] and $25 \leq Q_s \leq 80$ in the back-arc mantle of Central America, the Marianas and the Lau basin[49]. A recent experimental study[3] suggests that 0.2% of melt produces $Q_s = 48$. However, such a large effect of melt on Q_s is difficult to reconcile with long-period (>30 s) surface-wave observations of $Q_s = 80$ beneath the fast-spreading southern East Pacific Rise[20], where up to 1%–2% of melt is expected[50]. If the attenuation mechanism is melt squirt, then the dissipation peak may lie outside the seismic frequency band and cause little attenuation. Model calculations[51], long-period surface waves[20] and experiments[12] favour this interpretation. This is also supported by our long-period (100 s) global surface-wave tomographic models, which suggest that large V_s and Q_s reductions are not necessarily correlated[30,32]. For these reasons, we assume that, in the period range of surface waves (50–250 s), melt does not substantially affect attenuation and we neglect its effect on Q_s.

Temperature in the upper mantle

Our Q_s and V_s seismic models are interpreted using mineral-physics results[4,13]. These experimental results are valid at temperatures larger than 900 °C or 1,000 °C, which are reached at the base of the lithosphere and in the asthenosphere. The predictions of our model can be checked with respect to the well-known thermal behaviour of the cooling oceanic lithosphere[52,53], although this is pushing the model outside its applicability range. Supplementary Fig. 19a displays the temperature variations beneath the Pacific as a function of sea-floor age predicted from our seismic models using experimental results[4]. It demonstrates that even at depths shallower than 100 km, we retrieve the well-known age dependence of temperature in oceanic regions (we also pick up the cold signal of the west Pacific subductions at old ages). However, our temperature variations between the ridge and an old lithosphere (around 100 °C) are lower than those predicted by the plate-cooling model (250 °C at 75-km depth; Supplementary Fig. 19b). Supplementary Fig. 19c displays the quality factors that would be deduced from the plate-cooling model using the experimental results[4] used here. In the oceanic lithosphere, Q_s values much greater than 2,000 ($\ln Q_s > 7.6$) would be predicted, which cannot be retrieved by long-period seismology. The limitations of experimental data at low temperatures, together with the inability of surface-wave seismology to quantify precisely negligible attenuations, explain why we do not interpret results at depths shallower than 100 km. Supplementary Fig. 14g shows that, below the oceanic plates, our predicted temperatures beneath oceans are perfectly compatible with geodynamic and petrologic expectations. In agreement with our findings, under oceans, the average one-dimensional temperature profile is above the solidus[4] and the adiabat[54] in the depth range 100–200 km, where we predict partial melting. This overshoot of the temperature, above the adiabat, is found in all numerical simulations of mantle convection[55]. Under continents,

the temperature appears to be below the solidus[4] and the adiabat[54]. It reaches the adiabat at around 250-km depth (Supplementary Fig. 14g).

Compatibility of our results with electrical conductivity

Our results are consistent with the interpretations of several recent studies of electrical conductivity. In the depth range 100–150 km, the joint interpretation of electrical and seismic data[56] requires 0.3%–2.5% melt beneath the mid-Atlantic ridge, 1% or less melt beneath Hawaii and less than 5% melt beneath the East Pacific Rise, in good agreement with Fig. 3. We also confirm the absence of melt in the region of the NoMELT experiment[19], in agreement with conductivity data in this region[25]. Previous experimental results suggest that 0.3%–2% of hydrous basaltic melt can account for the observed electrical conductivity in the LVZ[27]. A more recent study[57] has refined these results by simultaneously measuring wave velocity and electrical conductivity on a simplified partial melt analogue. They conclude that the LVZ away from spreading ridges can be explained by 0.3%–0.8% volatile-bearing melt, the upper bound of our observations.

Implications for viscosity

The variation in viscosity as a function of melt content occurs in two steps[9]. First, the onset of melting has a strong effect on viscosity when a connected network of melt tubules is established. The viscosity η is expected to decrease by one or two orders of magnitude before the melt fraction φ reaches 0.1%. Second, for larger melt content, η decreases further[9], with $d\ln\eta/d\varphi = -26$; this effect is minor for the low melt content that we observe. The viscosity η should be one or two orders of magnitude lower under oceanic plates, where $\varphi \approx 0.3\%$, than under continents.

Data availability

The dataset generated during this study (three-dimensional V_s and Q_s models and melt-fraction models) is available as an IRIS data product at https://doi.org/10.17611/dp/emc.2020.dbrdnature.1. Source data are provided with this paper.

Code availability

Numerical modelling codes related to this paper are available from https://doi.org/10.17611/dp/emc.2020.dbrdnature.1. Most figures were created using open software GMT 4.5.13.

30. Adenis, A., Debayle, E. & Ricard, Y. Attenuation tomography of the upper mantle. *Geophys. Res. Lett.* **44**, 7715–7724 (2017).
31. Debayle, E. & Ricard, Y. A global shear velocity model of the upper mantle from fundamental and higher Rayleigh mode measurements. *J. Geophys. Res. Solid Earth* **117**, B10308 (2012).
32. Adenis, A., Debayle, E. & Ricard, Y. Seismic evidence for broad attenuation anomalies in the asthenosphere beneath the Pacific Ocean. *Geophys. J. Int.* **209**, 1677–1698 (2017).
33. Hirschmann, M. M. Mantle solidus: experimental constraints and the effects of peridotite composition. *Geochem. Geophys. Geosyst.* **1**, 1042 (2000).
34. Connolly, J. A. D. Computation of phase equilibria by linear programming: a tool for geodynamic modeling and its application to subduction zone decarbonation. *Earth Planet. Sci. Lett.* **236**, 524–541 (2005).
35. Karato, S. Importance of anelasticity in the interpretation of seismic tomography. *Geophys. Res. Lett.* **20**, 1623–1626 (1993).
36. Zaroli, C. Global seismic tomography using Backus-Gilbert inversion. *Geophys. J. Int.* **207**, 876–888 (2016).
37. Resovsky, J., Trampert, J. & der Hilst, R. D. Error bars for the global seismic Q profile. *Earth Planet. Sci. Lett.* **230**, 413–423 (2005).
38. French, S., Lekic, V. & Romanowicz, B. Waveform tomography reveals channeled flow at the base of the oceanic asthenosphere. *Science* **342**, 227–230 (2013).
39. Kustowski, B., Ekstrom, G. & Dziewonski, A. M. Anisotropic shear-wave velocity structure of the Earth's mantle: a global model. *J. Geophys. Res. Solid Earth* **113**, B06306 (2008).
40. Karato, S. I., Olugboji, T. & Park, J. Mechanisms and geologic significance of the mid-lithosphere discontinuity in the continents. *Nat. Geosci.* **8**, 509–514 (2015).
41. Ghahremani, F. Effect of grain boundary sliding on anelasticity of polycrystals. *Int. J. Solids Struct.* **16**, 825–845 (1980).
42. Hirschmann, M. M. & Stolper, E. M. A possible role for garnet pyroxenite in the origin of the "garnet signature" in MORB. *Contrib. Mineral. Petrol.* **124**, 185–208 (1996).
43. Lambart, S., Laporte, D. & Schiano, P. Markers of the pyroxenite contribution in the major-element compositions of oceanic basalts: review of the experimental constraints. *Lithos* **160–161**, 14–36 (2013).

44. Stixrude, L. & Lithgow-Bertelloni, C. Mineralogy and elasticity of the oceanic upper mantle: origin of the low-velocity zone. *J. Geophys. Res. Solid Earth* **110**, B03204 (2005).
45. Behn, M. D., Hirth, G. & Elsenbeck, J. R. Implications of grain size evolution on the seismic structure of the oceanic upper mantle. *Earth Planet. Sci. Lett.* **282**, 178–189 (2009).
46. Hirschmann, M. M. Water, melting, and the deep Earth H_2O cycle. *Annu. Rev. Earth Planet. Sci.* **34**, 629–653 (2006).
47. Faul, U. H., Fitz Gerald, J. D. & Jackson, I. Shear wave attenuation and dispersion in melt-bearing olivine polycrystals: 2. Microstructural interpretation and seismological implications. *J. Geophys. Res. Solid Earth* **109**, B06202 (2004).
48. Eilon, Z. C. & Abers, G. A. High seismic attenuation variation at a mid-ocean ridge reveals the distribution of deep melt. *Sci. Adv.* **3**, e1602829 (2017).
49. Abers, G. A. et al. Reconciling mantle attenuation-temperature relationships from seismology, petrology, and laboratory measurements. *Geochem. Geophys. Geosyst.* **15**, 3521–3542 (2014).
50. Dunn, R. A. & Forsyth, D. W. Imaging the transition between the region of mantle melt generation and the crustal magma chamber beneath the southern East Pacific Rise with short-period Love waves. *J. Geophys. Res. Solid Earth* **108**, 2352 (2003).
51. Hammond, W. C. & Humphreys, E. D. Upper mantle seismic wave attenuation: effects of realistic partial melt distribution. *J. Geophys. Res. Solid Earth* **105**, 10987–10999 (2000).
52. Turcotte, D. L. & Schubert, G. *Geodynamics: Applications of Continuum Physics to Geological Problems* Ch. 4 (John Wiley & Sons, 1982).
53. Stein, C. A. & Stein, S. A model for the global variation in oceanic depth and heat flow with lithospheric age. *Nature* **359**, 123–129 (1992).
54. Katsura, T. et al. Adiabatic temperature profile in the mantle. *Phys. Earth Planet. Inter.* **183**, 212–218 (2010).
55. Curbelo, J. et al. Numerical solutions of compressible convection with an infinite Prandtl number: comparison of the anelastic and anelastic liquid models with the exact equations. *J. Fluid Mech.* **873**, 646–687 (2019).
56. Pommier, A. & Garnero, E. J. Petrology-based modeling of mantle melt electrical conductivity and joint interpretation of electromagnetic and seismic results. *J. Geophys. Res. Solid Earth* **119**, 4001–4016 (2014).
57. Freitas, D., Manthilake, G., Chantel, J., Bouhifd, M. A. & Andrault, D. Simultaneous measurements of electrical conductivity and seismic-wave velocity of partially molten geological materials: effect of evolving melt texture. *Phys. Chem. Miner.* **46**, 535–551 (2019).

Author contributions E.D. and T.B. developed the concept for this paper. E.D. wrote the codes for the interpretation of the seismic models and drafted the manuscript. E.D. wrote the tomography code for V_s; Y.R. adapted this code for Q_s. T.B. contributed to the design of the figures and to writing the manuscript. Y.R. developed preliminary codes for interpreting the seismic models, contributed to all mineralogical aspects and to writing the manuscript. S.D. realized the tests of the effect of composition and contributed to writing the revised manuscript.

Competing interests The authors declare no competing interests.

Additional information
Supplementary information is available for this paper at https://doi.org/10.1038/s41586-020-2809-4.
Correspondence and requests for materials should be addressed to E.D.
Reprints and permissions information is available at http://www.nature.com/reprints.